EFFICIENT FINITE-DIFFERENCE ROOM ACOUSTICS SIMULATION INCORPORATING EXTENDED-REACTING ELEMENTS

Jan W. Smits

Independent Researcher
jws@possumstudios.com

ABSTRACT

A method is proposed that allows finite-difference (FD) simulation of room acoustics to incorporate extended-reacting porous elements without adding major computational cost. The porous elements are described by a rigid-frame equivalent fluid model and are incorporated into the time-domain formulation through auxiliary differential equations. By using a local staggered grid scheme for the boundaries of the porous elements, the method allows an efficient second-order scalar approach to be used for the uniform air and porous element interior regions that make up the majority of the computational domain. Both the scalar and staggered schemes are based on a face-centered cubic grid to minimize numerical dispersion. A software implementation running on GPU shows the accuracy of the method compared to a theoretical reference, and demonstrates the method's computational efficiency through a benchmark example.

1. INTRODUCTION

The acoustic simulation of enclosed spaces is important in many applications, from the architectural design of performance halls and recording studios to the production of synthetic audio effects for music, cinema and virtual acoustics. In large rooms, such as performance halls, these simulations are usually performed using a geometrical acoustics approach such as ray or beam tracing [1]. In smaller rooms wave-based methods become necessary to accurately represent diffraction and modal behavior, but unfortunately such methods are computationally intensive. A range of wave-based methods has been applied to this problem, with finite difference (FD) [2] [3] [4] amongst the most popular, thanks in part to its suitability for implementation on GPU [5] [6] [7] [8].

One of the challenges in room acoustics is to accurately model the impact of various absorptive elements and surfaces in a room. This can include furniture and wall and floor coverings, as well as treatment panels or modules that are purposely added to alter the acoustics of the space. The behavior of such elements is often approximated with a locally reacting boundary assumption that simplifies the analysis [9] [10], but which may introduce significant errors. Problems appear for example when absorbing panels are present that have significant air gaps [11] [12] [13]. A more accurate approach is then to compute the 3-D acoustic propagation inside of any porous media as part of the overall simulation.

FD methods have been described that calculate such extended reaction in 2-D [14] and 3-D [15], making use of idealized models for the porous medium and conventional staggered Cartesian grids. More recently, 3-D discontinous Galerkin methods have been described that allow for a more general equivalent-fluid model (EFM) [16] [17], whereas EFM-based FD methods have been shown in up to two dimensions [18] [19]. Meanwhile, non-Cartesian FD approaches have been demonstrated that improve computational efficiency [20] [21] [22], but these schemes have not yet been adapted to allow the modeling of extended reaction.

The aim of this paper is to describe a FD method that extends the non-Cartesian face-centered cubic (FCC) scheme to include the simulation of porous media described by a general frequency-dependent EFM, thus enabling the simulation of extended-reacting elements with higher computational and memory efficiency than previous approaches. To the author's knowledge, this is the first time that a wave-based room acoustics method incorporating extended reaction is demonstrated at full audio bandwidth.

The paper is organized as follows. Section 2 describes the background of compact FD schemes, including a short discussion on dispersion error and computational efficiency. Section 3 then describes the internal porous volume update that is part of the new approach, and this is followed by a description of the porous volume boundary updates in section 4.2. The latter section also details the staggered FCC grid that is used at the boundaries. Section 5 shows results obtained through a GPU-based software implementation, and section 6 provides a short summary of conclusions.

2. FINITE-DIFFERENCE SCHEMES

2.1. Yee scheme

Room acoustics analysis usually starts with the linearized equations of continuity and conservation of momentum

$$\partial_t p = -\rho_0 c^2 \nabla \cdot \boldsymbol{v} \tag{1}$$

$$\rho_0 \partial_t \boldsymbol{v} = -\nabla p \tag{2}$$

where p represents the scalar pressure field, and $\boldsymbol{v}$ the velocity vector field. The constants ρ_0 and c represent the static fluid density ($\mathrm{kg/m^3}$) and propagation speed of sound ($\mathrm{m/s}$) respectively.

To achieve satisfactory results at higher frequencies, viscothermal losses can be incorporated through a post-processing step as described in [23] or [24], which avoids impacting the complexity of the computations through addition of a loss term in (2).

A common approach to solving the first-order system of Eqs.(1) (2) is to discretize them on a so-called Yee grid [25], where the pressure and particle velocities are interlaced in both space and time [4], [2]:

$$\delta_{t+} \underline{p}_{\boldsymbol{i}}^{n} = -\rho_0 c^2 (\delta_{\boldsymbol{x}-})^T \underline{\boldsymbol{v}}_{\boldsymbol{i}+\frac{1}{2}}^{n+\frac{1}{2}} \tag{3}$$

$$\rho_0 \delta_{t-} \underline{\boldsymbol{v}}_{\boldsymbol{i}+\frac{1}{2}}^{n+\frac{1}{2}} = -\delta_{\boldsymbol{x}+} \underline{p}_{\boldsymbol{i}}^{n} \tag{4}$$

The underlined variables in these formulas denote grid functions that approximate their continuous counterparts:

$$\underline{p}_{\boldsymbol{i}}^{n} \approx p(\boldsymbol{i}h, nk) \tag{5}$$

$$\underline{\boldsymbol{v}}_{\boldsymbol{i}+\frac{1}{2}}^{n+\frac{1}{2}} \approx \boldsymbol{v}_{\left((i_x+\frac{1}{2})h,(i_y+\frac{1}{2})h,(i_z+\frac{1}{2})h,nk\right)} \tag{6}$$

where k and h are the temporal and spatial grid steps respectively, and $\boldsymbol{i}$ and n are discrete indices:

$$\boldsymbol{i} := (i_x, i_y, i_z) \in \mathbb{Z}^3, \quad n \in \mathbb{Z}^+ \tag{7}$$

The operators δ_{t+} and δ_{t-} are first-order forward and backward difference operators defined here as

$$\delta_{t+}\underline{p}^{n} := \frac{1}{k}\left(\underline{p}^{n+1} - \underline{p}^{n}\right), \quad \delta_{t-}\underline{p}^{n} := \frac{1}{k}\left(\underline{p}^{n} - \underline{p}^{n-1}\right) \tag{8}$$

and $\delta_{\boldsymbol{x}+}$ and $\delta_{\boldsymbol{x}-}$ stand for spatial difference (vector) operators. Throughout this paper, bold emphasis will be used to distinguish vector quantitites and operators from scalar ones.

2.2. Standard leapfrog scheme

Eqs. (1) and (2) can also be combined to form a scalar wave equation for the pressure:

$$\partial_{tt} p = c^2 \Delta p \tag{9}$$

This second-order equation can then be discretized as

$$\delta_{tt}\underline{p} = c^2 \delta_{\Delta}\underline{p} \tag{10}$$

where δ_{tt} is a second-order time-difference operator defined as

$$\delta_{tt}\underline{p}_{\boldsymbol{i}}^{n} = \frac{1}{k^2}(\underline{p}_{\boldsymbol{i}}^{n+1} - 2\underline{p}_{\boldsymbol{i}}^{n} + \underline{p}_{\boldsymbol{i}}^{n-1}) \tag{11}$$

and δ_{Δ} is a discrete Laplacian operator

$$\delta_{\Delta}\underline{p}_{\boldsymbol{i}}^{n} = \frac{1}{h^2}\left(Q_{\boldsymbol{i}}^{n} - 6\underline{p}_{\boldsymbol{i}}^{n}\right) \tag{12}$$

with $Q_{\boldsymbol{i}}^{n}$ representing the sum of the nearest neighbors of $\underline{p}_{\boldsymbol{i}}^{n}$:

$$Q_{\boldsymbol{i}}^{n} := \underline{p}_{\boldsymbol{i}+\boldsymbol{e}_x}^{n} + \underline{p}_{\boldsymbol{i}-\boldsymbol{e}_x}^{n} + \underline{p}_{\boldsymbol{i}+\boldsymbol{e}_y}^{n} + \underline{p}_{\boldsymbol{i}-\boldsymbol{e}_y}^{n} + \underline{p}_{\boldsymbol{i}+\boldsymbol{e}_z}^{n} + \underline{p}_{\boldsymbol{i}-\boldsymbol{e}_z}^{n} \tag{13}$$

Substituting (11) and (12) in (10) and using the Courant number $\lambda := ck/h$, leads to the scalar update equation

$$\underline{p}_{\boldsymbol{i}}^{n+1} = -\underline{p}_{\boldsymbol{i}}^{n-1} + (2 - 6\lambda^2)\underline{p}_{\boldsymbol{i}}^{n} + \lambda^2 Q_{\boldsymbol{i}}^{n} \tag{14}$$

This formula is often referred to as the "standard leapfrog" scheme [26], abbreviated as SLF. In [27] it is shown that this scheme and the Yee scheme are equivalent, and produce results that are identical to within machine precision. The SLF scheme is usually preferable over the Yee scheme, because it requires less computer memory and fewer computational operations [27].

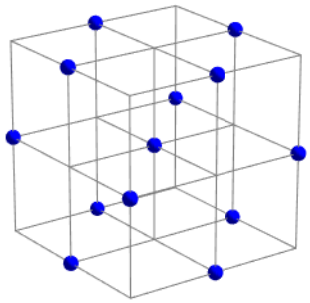

Figure 1: *Pressure field positions of a face-centered cubic (FCC) grid, shown in relation to an associated Cartesian grid.*

2.3. Face-centered cubic scheme

Other schemes for the wave equation can be formulated by considering expanded stencils for the Laplacian operator [20]. A compact stencil of particular interest for room acoustics is the face-centered cubic (FCC) stencil [28] [21], so called because its nodes lie on a non-Cartesian face-centered cubic grid, which is defined by:

$$\boldsymbol{i} := (i_x, i_y, i_z) \in \{\mathbb{Z}^3 : (i_x + i_y + i_z) \pmod 2 = 0\} \tag{15}$$

From the illustration in Figure 1 it can be seen that each node on the FCC grid is surrounded by twelve nearest neighbors, resulting in a 13-point compact Laplacian stencil. If we use the vector $\boldsymbol{l}_m$ to represent the relative coordinates of the nearest neighbors of a given grid node, the Laplacian operator for the FCC scheme can be written as:

$$\delta_{\Delta}\underline{p}_{\boldsymbol{i}}^{n} = \frac{1}{4h^2}\left(\sum_{m=1}^{12} \underline{p}_{\boldsymbol{i}+\boldsymbol{l}_m}^{n} - 12\underline{p}_{\boldsymbol{i}}^{n}\right) \tag{16}$$

By substituting $\underline{P}_{\boldsymbol{i}}^{n} := \sum_{m=1}^{12} \underline{p}_{\boldsymbol{i}+\boldsymbol{l}_m}^{n}$, this can be simplified to:

$$\delta_{\Delta}\underline{p}_{\boldsymbol{i}}^{n} = \frac{1}{4h^2}\left(\underline{P}_{\boldsymbol{i}}^{n} - 12\underline{p}_{\boldsymbol{i}}^{n}\right) \tag{17}$$

Then, using the second-order time operator of (11), the update equation for the FCC scheme follows as:

$$\underline{p}_{\boldsymbol{i}}^{n+1} = \frac{\lambda^2}{4}(\underline{P}_{\boldsymbol{i}}^{n} - 12\underline{p}_{\boldsymbol{i}}^{n}) + 2\underline{p}_{\boldsymbol{i}}^{n} - \underline{p}_{\boldsymbol{i}}^{n-1} \tag{18}$$

The principal benefit of the FCC scheme lies in the fact that it exhibits higher computational efficiency than other compact FD schemes, as shown by Hamilton and Bilbao in [21]. To achieve a fair comparison, the analysis in the reference maximizes the grid steps in each scheme for a given numerical dispersion error, while also satisfying the stability constraint of each method.

A recent study [29] finds that the threshold of human perception lies around 2% dispersion error for spaces with shorter echo times, as typically found in small acoustically treated spaces such as mixing rooms. At this error level, the analysis in [21] finds that the FCC scheme is 11.3 times more efficient than the SLF scheme, and this ratio will be around double when FCC is compared to the Yee scheme [27]. Because all previous FD methods for extended reaction have been based on the Yee scheme [14] [15] [18] [19], this provides clear motivation for the development of an FCC-based approach .

3. EXTENDED-REACTION FD SCHEME

3.1. Equivalent fluid model

For the purpose of room acoustics, the propagation of sound in porous media is commonly described with a rigid-frame equivalent-fluid model (EFM) [11]. In this approximation, the frame of the material is assumed motionless, and the air inside it is replaced macroscopically by an equivalent free fluid with a complex bulk modulus and effective density that both depend on frequency. The acoustic equations for the domain Ω_P of the porous volume, can then be formulated in the frequency domain as

$$j\omega\hat{p} = -\hat{K}(\omega)\nabla\cdot\hat{\boldsymbol{v}}, \quad \boldsymbol{x}\in\Omega_P \tag{19}$$

$$j\omega\hat{\boldsymbol{v}} = -\hat{R}(\omega)\nabla\hat{p}, \quad \boldsymbol{x}\in\Omega_P \tag{20}$$

Here, $\hat{\boldsymbol{v}}$ and $\hat{p}$ denote Fourier-transforms of the corresponding time-domain variables. The complex frequency-dependent quantities $\hat{K}(\omega)$ and $\hat{R}(\omega)$ represent the EFM estimates for the medium's effective bulk modulus in N/m^2 and the inverse of its effective density in m^3/kg respectively. Combining (19) and (20) leads to the Helmholtz equation

$$\omega^2\hat{p} = -\hat{R}(\omega)\hat{K}(\omega)\Delta\hat{p}, \quad \boldsymbol{x}\in\Omega_P \tag{21}$$

A primary condition for the validity of the EFM is that wavelengths are much larger than the characteristic dimensions of the pores [11].

A variety of EFMs have been proposed based on empirical and/or phenomenological justifications; see for example sections 2.5, 5.4 and 5.5 of [11]. For the results in this paper, the Allard-Champoux model was used, described in [30]. With ambient conditions defined by a static pressure $\rho_0 = 1.2\mathrm{kg/m^3}$, a Prandtl number of 0.702, an adiabatic index of 1.40 and a static pressure of 101,320 N/m^2, Eqs. (5) and (6) of [30] provide the model formulas as:

$$\hat{R}(\omega)^{-1} = 1.2 + \left(-0.0364X^{-2} - j0.1144X^{-1}\right)^{1/2} \tag{22}$$

$$\hat{K}(\omega) = 101320\frac{j29.64 + \left(2.82X^{-2} + j24.9X^{-1}\right)^{1/2}}{j21.17 + \left(2.82X^{-2} + j24.9X^{-1}\right)^{1/2}} \tag{23}$$

The intermediate variable X in these formulas is defined as $X := \rho_0 f/\sigma$, with $f = \omega/2\pi$ as the frequency in Hz, and σ representing the flow resistivity of the material in $\mathrm{Nm^{-4}s}$.

3.2. Auxiliary differential equations (ADE) method

In order to solve either (21) or the combination of (19) and (20) in the time domain, the method of auxiliary differential equations (ADE method) will be used, described in [31] and previously applied in [16], [17], [32] and [19], amongst others.

The ADE method consists in approximating the inverse effective density and effective bulk modulus with limited-order rational functions in the frequency domain, then formulating the inverse Fourier-transformed system with a set of additional state variables called accumulators, and determining these accumulators through a set of auxiliary differential equations that are solved alongside the acoustical equation(s). The benefit of this approach is that it avoids computationally expensive convolutions in the time domain, instead performing a limited number of additional state variable computations.

Due to the passive and non-resonant nature of conventional porous materials, it is sufficient to approximate the equivalent fluid properties with only real poles [32], such that the partial fraction expansions can be written as follows

$$\hat{K} \approx \hat{K}_\infty + \sum_{m=1}^{\mathcal{M}_K}\frac{A_{K,m}}{\eta_{K,m} + j\omega} \tag{24}$$

$$\hat{R} \approx \hat{R}_\infty + \sum_{m=1}^{\mathcal{M}_R}\frac{A_{R,m}}{\eta_{R,m} + j\omega} \tag{25}$$

for $\mathcal{M}_K$ and $\mathcal{M}_R$ fractions respectively. The poles $(-\eta)$, residues A, and high-frequency limit values $\hat{K}_\infty$, $\hat{R}_\infty$ in this approximation are found through a fitting procedure such as the method of vector-fitting [33] used here. For stability, the poles should be constrained to be negative or zero ($\eta \geq 0$) [1]

It will also be useful to approximate the product of $\hat{R}$ and $\hat{K}$, in a similar manner:

$$\hat{R}\hat{K} \approx \hat{R}_\infty\hat{K}_\infty + \sum_{m=1}^{\mathcal{M}_{RK}}\frac{A_{RK,m}}{\eta_{RK,m} + j\omega} \tag{26}$$

Using this expression, an approximation for the inverse Fourier transform of (21) can be obtained as

$$\partial_{tt}p(t) \approx \hat{R}_\infty\hat{K}_\infty\Delta p(t) + \sum_{m=1}^{\mathcal{M}_{RK}} A_{RK,m}\phi_{RK,m}(t) \tag{27}$$

where $\phi_{RK,m}$ are accumulator variables that satisfy the auxiliary differential equations defined as:

$$\partial_t\phi_{RK,m} + \eta_{RK,m}\phi_{RK,m} = \Delta p, \forall m \in [1, \mathcal{M}_{RK}] \tag{28}$$

3.3. Porous medium update in FCC scheme

Let us now define three non-overlapping sets of nodes for the finite-difference grid. An interior porous volume set $\mathcal{P}_p$ is defined as the set of grid nodes that are inside of the porous region and for which all the nearest neighbors are also inside the region. The air interior set $\mathcal{P}_a$ similarly contains all nodes that are in air and whose neighbors are in air also. Finally, the boundary set $\mathcal{P}_b$ consists of all nodes which are separated from at least one neighbor by a porous volume boundary.

For the nodes in $\mathcal{P}_p$, a finite-difference update can then be derived in two steps. In the first step, grid functions $\underline{\phi}_{RK,m}$ are computed to approximate the continuous accumulators $\phi_{RK,m}$ by evaluating a discretization of (28) at each time step:

$$\underline{\phi}^{n+\frac{1}{2}}_{RK,m,\boldsymbol{i}} = \frac{(2 - k\eta_{RK,m})}{(2 + k\eta_{RK,m})}\underline{\phi}^{n-\frac{1}{2}}_{RK,m,\boldsymbol{i}} + \frac{2k}{(2 + k\eta_{RK,m})}\delta_\Delta\underline{p}^n_{\boldsymbol{i}}, \quad \forall m \in [1, \mathcal{M}_{RK}] \tag{29}$$

where δ_Δ is the discrete Laplacian operator from (16), and ∂_t has been approximated with the δ_{t+} operator defined in (8).

For the second step, an update formula of the pressure values is derived from (27) by replacing p with the grid function $\underline{p}$, applying

[1] Note that the $(e^{+j\omega t})$ time convention used here is opposite that of the negative time convention used in [31], explaining the different sign appearing in the fraction denominators in Eqs. (24) (25) (26).

the second-order operators defined in (11) and (16), and interpolating between $\underline{\phi}_{RK,m,\boldsymbol{i}}^{n+\frac{1}{2}}$ and $\underline{\phi}_{RK,m,\boldsymbol{i}}^{n-\frac{1}{2}}$ to ensure that the accumulator term is centered at time index n:

$$\underline{p}_{\boldsymbol{i}}^{n+1} = \frac{k^2 \hat{R}_\infty \hat{K}_\infty}{4h^2}(\underline{P}_{\boldsymbol{i}}^{n} - 12\underline{p}_{\boldsymbol{i}}^{n}) + 2\underline{p}_{\boldsymbol{i}}^{n} - \underline{p}_{\boldsymbol{i}}^{n-1} + \frac{k^2}{2}\sum_{m=1}^{\mathcal{M}_{RK}} A_{RK,m}\left(\underline{\phi}_{RK,m,\boldsymbol{i}}^{n+\frac{1}{2}} + \underline{\phi}_{RK,m,\boldsymbol{i}}^{n-\frac{1}{2}}\right) \quad (30)$$

4. POROUS-VOLUME BOUNDARY UPDATE

4.1. Staggered FCC grid

Because the material properties are discontinuous across boundaries of the porous volume, the wave-equation based approach of section 3.3 can not be used for the nodes in $\mathcal{P}_b$. Instead, a staggered scheme will be used that makes it possible to formulate a finite-difference approximation of the first-order system of Eqs. (19) (20). This scheme is part of a family of staggered formulations that can be derived from a finite-volume framework for isohedral cell shapes, described in [34].

For this study, the scheme will be described using a staggered grid that is created by complementing an FCC pressure grid with a set of six velocity subgrids. The velocity subgrids are each created by translating the nodes $\boldsymbol{i}$ of the FCC grid with one of six grid offset vectors $\boldsymbol{j}_l$, defined as

$$\begin{aligned} \boldsymbol{j}_1 &:= \frac{1}{2}\begin{pmatrix}1\\1\\0\end{pmatrix}, \quad \boldsymbol{j}_2 := \frac{1}{2}\begin{pmatrix}0\\1\\1\end{pmatrix}, \quad \boldsymbol{j}_3 := \frac{1}{2}\begin{pmatrix}1\\0\\1\end{pmatrix} \\ \boldsymbol{j}_4 &:= \frac{1}{2}\begin{pmatrix}1\\-1\\0\end{pmatrix}, \quad \boldsymbol{j}_5 := \frac{1}{2}\begin{pmatrix}0\\1\\-1\end{pmatrix}, \quad \boldsymbol{j}_6 := \frac{1}{2}\begin{pmatrix}1\\0\\-1\end{pmatrix} \end{aligned} \quad (31)$$

Scalar velocity grid functions $\underline{v}_{l,\boldsymbol{i}+\boldsymbol{j}_l}$ can be defined on each of these six subgrids to approximate the value of the velocity field in the direction of its associated grid vector:

$$\underline{v}_{l,\boldsymbol{i}+\boldsymbol{j}_l} \approx \boldsymbol{v}(h\boldsymbol{i} + h\boldsymbol{j}_l) \cdot (\boldsymbol{j}_l/\|\boldsymbol{j}_l\|) \quad (32)$$

The staggered grid formed by the combination of these subgrids is depicted in Figure 2. Similarly to the Yee grid, the velocity points are located at the midpoint between adjacent pressure nodes and only a single component is stored for each velocity point.

Using this grid, we can now define a discrete velocity divergence operator as

$$(\delta_{\boldsymbol{x}-} \cdot \underline{v})_{\boldsymbol{i}} := \frac{1}{2\sqrt{2}h}\sum_{l=1}^{6}\left(\underline{v}_{l,\boldsymbol{i}+\boldsymbol{j}_l} - \underline{v}_{l,\boldsymbol{i}-\boldsymbol{j}_l}\right) \quad (33)$$

and a discrete gradient operator for the pressure as

$$\left(\delta_{\boldsymbol{x}+}\underline{p}_{\boldsymbol{i}}\right)_l := \frac{1}{\sqrt{2}h}\left(\underline{p}_{\boldsymbol{i}+2\boldsymbol{j}_l} - \underline{p}_{\boldsymbol{i}}\right) \quad (34)$$

Applying these operators to (1) and (2) results in a staggered FD scheme as follows:

$$\delta_{t+}\underline{p}_{\boldsymbol{i}}^{n+1} = -\frac{\rho_0 c^2}{2\sqrt{2}h}\sum_{l=1}^{6}\left(\underline{v}_{l,\boldsymbol{i}+\boldsymbol{j}_l}^{n+\frac{1}{2}} - \underline{v}_{l,\boldsymbol{i}-\boldsymbol{j}_l}^{n+\frac{1}{2}}\right) \quad (35)$$

$$\delta_{t-}\underline{v}_{l,\boldsymbol{i}+\boldsymbol{j}_l}^{n+\frac{1}{2}} = -\frac{1}{\rho_0\sqrt{2}h}\left(\underline{p}_{\boldsymbol{i}+2\boldsymbol{j}_l}^{n} - \underline{p}_{\boldsymbol{i}}^{n}\right) \quad (36)$$

The equivalence derived more generally in [34] can be verified by applying a δ_{t-} operator to (35) and substituting (36). This leads to the following second-order FD expression:

$$\delta_{t-}\delta_{t+}\underline{p}_{\boldsymbol{i}}^{n+1} = \frac{c^2}{4h^2}\sum_{l=1}^{6}\left(\left(\underline{p}_{\boldsymbol{i}+2\boldsymbol{j}_l}^{n} + \underline{p}_{\boldsymbol{i}-2\boldsymbol{j}_l}^{n}\right) + 12\underline{p}_{\boldsymbol{i}}^{n}\right) \quad (37)$$

which, upon substitution of (8) for the difference operators results in the same expression as (18).

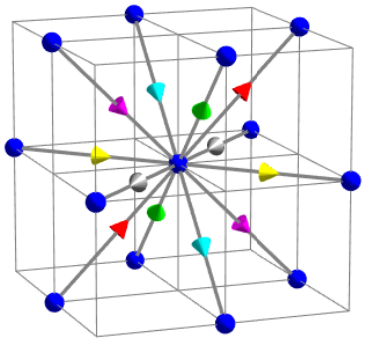

Figure 2: *Depiction of the local staggered face-centered (FCC) grid. The blue spheres denote the pressure subgrid, and different colors are used to distinguish each of the six velocity subgrids. For visual simplicity the plot only shows the twelve velocity nodes that are directly adjacent to the central pressure node.*

4.2. Staggered-scheme boundary update

The system to be solved on the boundary is obtained by applying the ADE method to the inverse Fourier transforms of Eqs. (19) and (20), with use of the rational approximations (24) and (25):

$$\partial_t p = -\hat{K}_\infty \nabla \cdot \boldsymbol{v} - \sum_{m=1}^{\mathcal{M}_K} A_{K,m}\phi_{K,m} \quad (38)$$

$$\partial_t \boldsymbol{v} = -\hat{R}_\infty \nabla p - \sum_{m=1}^{\mathcal{M}_R} A_{R,m}\boldsymbol{\phi}_{R,m} \quad (39)$$

where

$$\partial_t \phi_{K,m} + \eta_{K,m}\phi_{K,m} = \nabla \cdot \boldsymbol{v}, \quad \forall m \in [1, \mathcal{M}_K] \quad (40)$$

and

$$\partial_t \boldsymbol{\phi}_{R,m} + \eta_{R,m}\boldsymbol{\phi}_{R,m} = \nabla p, \quad \forall m \in [1, \mathcal{M}_R] \quad (41)$$

A FD formulation can now be obtained for the pressure nodes in $\mathcal{P}_b$ by applying the divergence and gradient operators from (33) and (34) to Eqs. (38) thru (41), resulting in

$$\underline{p}_{\boldsymbol{i}}^{n+1} = \underline{p}_{\boldsymbol{i}}^{n} - k\hat{K}_\infty\left(\delta_{\boldsymbol{x}-} \cdot \underline{v}^{n+\frac{1}{2}}\right)_{\boldsymbol{i}} - \frac{k}{2}\sum_{m=1}^{\mathcal{M}_K} A_{K,m}\left(\underline{\phi}_{K,m,\boldsymbol{i}}^{n+1} + \underline{\phi}_{K,m,\boldsymbol{i}}^{n}\right) \quad (42)$$

$$\underline{v}_{l,\boldsymbol{i}+\boldsymbol{j}_l}^{n+\frac{1}{2}} = \underline{v}_{l,\boldsymbol{i}+\boldsymbol{j}_l}^{n-\frac{1}{2}} - k\hat{R}_\infty \left(\delta_{\boldsymbol{x}+} \underline{p}_{\boldsymbol{i}}^{n}\right)_l - \frac{k}{2} \sum_{m=1}^{\mathcal{M}_R} A_{R,m} \left(\underline{\phi}_{R,m,\boldsymbol{i},l}^{n+\frac{1}{2}} + \underline{\phi}_{R,m,\boldsymbol{i},l}^{n-\frac{1}{2}}\right) \quad (43)$$

and the associated accumulator updates

$$\underline{\phi}_{K,m,\boldsymbol{i}}^{n+1} = \frac{(2-k\eta_{K,m})}{(2+k\eta_{K,m})} \underline{\phi}_{K,m,\boldsymbol{i}}^{n} + \frac{2k}{(2+k\eta_{K,m})} \left(\delta_{\boldsymbol{x}-} \cdot \underline{\boldsymbol{v}}^{n+\frac{1}{2}}\right)_{\boldsymbol{i}}, \quad \forall m \in [1, \mathcal{M}_K] \quad (44)$$

$$\underline{\phi}_{R,m,\boldsymbol{i},l}^{n+\frac{1}{2}} = \frac{(2-k\eta_{R,m})}{(2+k\eta_{R,m})} \underline{\phi}_{R,m,\boldsymbol{i},l}^{n-\frac{1}{2}} + \frac{2k}{(2+k\eta_{R,m})} \left(\delta_{\boldsymbol{x}+} \underline{p}_{\boldsymbol{i}}^{n}\right)_l, \quad \forall m \in [1, \mathcal{M}_R] \quad (45)$$

In these equations, the accumulator variables for the continuity and momentum equations are shifted by $k/2$ from each other in time in order to ensure that both updates remain centered.

Figure 3 depicts a 2-D cross section of the grid, illustrating the transition between the regular FCC grids used in the air and porous volume sections, and the staggered FCC grid used at the boundaries. The local (staggered) grid needs to include at a minimum all pressure nodes that are separated from one or more of their nearest neighbors by a porous-volume boundary. For each of these pressure nodes, the evaluation of (42) requires that all the adjacent velocity values are computed and stored as well.

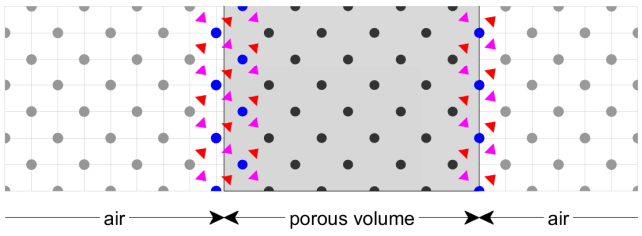

Figure 3: *2-D cross section showing the local staggered grid at the boundaries of a porous volume. The blue spheres indicate the pressure nodes of the local grid ($\mathcal{P}_b$), and the red and violet triangles indicate the associated velocity nodes in the viewing plane. The internal pressure nodes of the air ($\mathcal{P}_a$) and porous volumes ($\mathcal{P}_p$) are shown in light and dark grey respectively. A raster in the background shows how the nodes are positioned relative to the Cartesian grid spacing (h).*

4.3. Rigid boundary conditions

At the edges of the domain, rigid boundary conditions are applied that enforce zero particle velocity normal to the boundary: $v_\perp = 0$. In the domain covered by the staggered grid this is implemented simply by setting the corresponding velocity values resulting from (43) to zero, prior to the evaluation of (42). In the air and porous volume internal domains, the boundary condition is implemented by modifying the Laplacian operator: any "ghost points" that are located across from a boundary are removed from the summation in (16), and for each removal, the constant factor 12 on the right is reduced by 1.

5. PRACTICAL RESULTS

5.1. Implementation

The method described in this paper was implemented as a C++ computer program, making use of the CUDA programming interface to access GPU compute capabilities. New CUDA Kernels were developed for the updates (30) (29) on the porous volume internal domain and updates (35) (36) (44) (45) along with updates for the rigid boundary conditions adjacent to porous volumes. Kernels for the air update (18) and for rigid boundary conditions next to the air domain were borrowed from Hamilton's open-source FD program named PFFDTD to save development effort [35].

In order to facilitate efficient GPU data access on the staggered grid, linked data structures were constructed that avoid expensive spatial search operations. The preparation of this data from input geometry was implemented making use of the OpenVDB library of sparse volumetric data structures and tools [36].

5.2. Comparison against theory

An absorber configuration is considered at normal and 45° angles of incidence θ, as shown in Fig. 4. The configuration consists of a 10cm thick porous panel that is separated by a 20cm thick air gap from a rigid boundary. The height and width of the domain are both 16m, and its length is 5.3m for the case of normal incidence, and 18.3m for the oblique incidence case. Initial conditions are set up to generate a plane wave with a 4cm wide raised cosine shape, starting at 10cm to the left of the left-most absorber edge. The pressure is computed at the midpoint on the surface of the porous panel and is truncated in time to avoid contamination by spurious reflections due to the finite domain and absorber sizes. The grid step (h) is 1 cm. The porous medium properties are defined by Eqs. (22) (23) with $\rho_0 = 1.2\text{kg/m}^3$ and a flow resistivity value of $\sigma = 10,000\text{Nm}^{-4}\text{s}$, which is situated in the typical range for commonly used reticulated foams.

The coefficients of Eqs. (24) (25) (26) were found by using the method of vector fitting [33], in which two poles were used to fit each of $\hat{R}$ and $\hat{K}$, and three poles were used to fit the product $\hat{R}\hat{K}$. It was found that for the above parameter values, these fit orders were sufficient to fit the Allard-Champoux model within 0.32% maximum relative error over a frequency range of 20 to 4,000 Hz.

In order to compute the surface impedance of the absorber, an incident-wave pressure p_i is first computed by removing the absorber from the simulation. This response is than subtracted from the response with the absorber to yield the reflected-wave pressure p_r. By taking the FFT of both p_r and p_i and then dividing the two, a frequency-domain reflection coefficient $\hat{R}$ is found, from which the surface impedance $\hat{Z}$ and absorption coefficient α can be computed through [11]:

$$\hat{Z} = \frac{\rho_0 c \left(1+\hat{R}\right)}{\cos\theta \left(1-\hat{R}\right)} \quad (46)$$

and

$$\alpha = 1 - ||\hat{R}||^2 \quad (47)$$

For comparison of the simulation against theory, an exact analytical formulation is used for the surface impedance of multilayered fluids at oblique incidence, provided in section 3.4 of [11]. The results along with the theoretical reference are shown in Figs.

5 and 6 for the incidence angles of 0° and 45° respectively. In both cases the absorption shows a close match to the theory.

A brief comment should be made here about errors due to the non-conforming grid, also referred to as staircase errors. Generally, an issue arises due to staircasing when absorbing local-reacting boundary conditions are applied, resulting in significant angle-dependent errors in the energy absorption, that do not reduce when the grid step is refined [10]. These errors are due to incorrect effective surface-area of the applied boundary condition. Because the extended-reaction absorber modeling described here is volumetric in nature, it does not exhibit this type of error, as supported by the fact that both modeled angles yield absorptions that are close to the theoretical values. On the other hand, a new type of error may appear when modeling thin structures, because the non-conforming grid can cause errors in the effective absorber thickness. Further analysis of this limitation should be conducted as part of follow-up work.

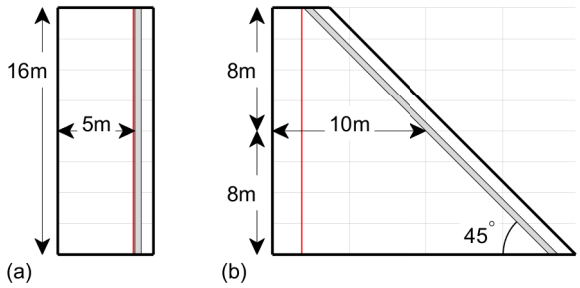

Figure 4: *Geometry of the validation test with gapped absorber. (a) Test case for normal incidence. (b) Test case for* 45° *incidence. The porous absorber thickness (10cm) and air gap size (20cm) are shown exaggerated four times for visual clarity. The thick lines around the outside represent rigid boundary conditions. The red vertical lines mark the position of the plane wave initialization, 10cm to the left of the left-most absorber dimension.*

5.3. Efficiency results

As a benchmark case for the computational and memory efficiency of the method, a configuration was used consisting of a rectangular room with a 10 cm thick porous panel hanging 20 cm below the ceiling, as well as a vertical free-standing porous panel with dimensions of 1.8 m height by 1.2 m width and 20 cm thickness. Dimensions of the room are $5\mathrm{m} \times 5\mathrm{m} \times 4\mathrm{m}$ yielding a total volume of 100 m^3, and the simulation was run at resolutions of $h = 10.0\mathrm{mm}$ and $h = 3.07\mathrm{mm}$ in terms of the Cartesian grid step, giving a maximum of 2% numerical dispersion for frequencies up to 6.2 kHz and up to 20 kHz respectively.

Figure 7 shows an early-time visualization of the wavefront propagation, where a point-source is used with a 20 cm wide single-cycle sine excitation. Partial transmission, reflection, and refraction of the pressure signal are visible at the porous barriers as expected.

The performance results for this benchmark model are summarized in Table 1 for impulse-response simulations with a duration of $1s$, executed on a RTX A5000 GPU with 24GB video RAM. The timing data shows that the addition of the extended-reaction modeling results in a moderate additional cost in compute,

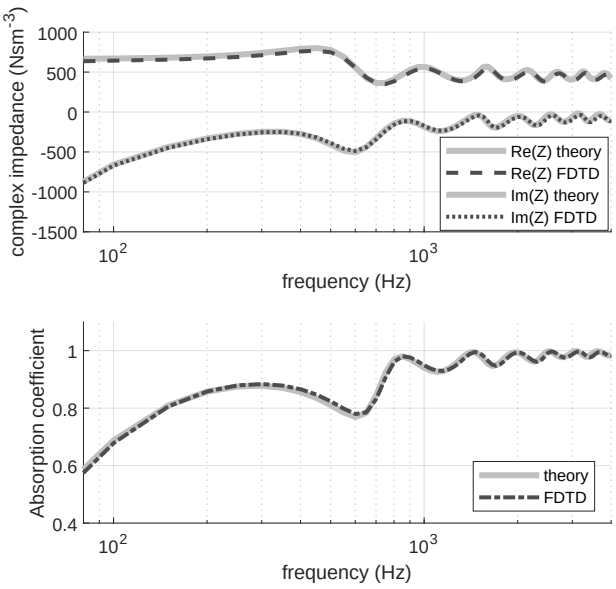

Figure 5: *Simulated impedance and absorption coefficient at interface of absorber for a normal incidence plane wave, with comparison to theory.*

with 27% of the total GPU time being spent on porous medium updates in the full-bandwidth simulation, and 45% in the 6.2 kHz case. The results imply that, for smaller-sized rooms at least, it is feasible with this method to perform simulations up to full audio frequency range on a single workstation GPU.

Experimentally, the porous volume updates were found to behave in a stable manner at least up to the stability limit $ck/h \leq 1$ of the FCC scheme in air. This result aligns with the fact that the wave propagation velocity in porous volumes is lower than in air. A formal analysis of the stability conditions should be undertaken as follow-up work.

6. CONCLUSIONS AND FUTURE WORK

In this paper a new finite-difference (FD) method was described for the computation of acoustical impulse responses in rooms that include rigid-frame porous media. By combining second-order face-centered cubic (FCC) updates in the uniform subdomains with a staggered grid formulation on the boundaries, the method makes it possible to include extended-reaction effects at only a limited extra computational cost.

An experimental GPU-based software implementation was described, and results were presented. A theoretical test case was shown to provide validation for the accuracy of the method and a benchmark case was used to quantify the computational and memory performance. The benchmark results demonstrate that it is possible to compute extended reaction in a small room up to full audio-bandwidth on a single GPU.

The method behaved in a stable manner during the experimental tests, however, a formal analysis of the stability conditions should be performed as part of follow-up work. Future work should also quantify the impact of stairstep error when modeling thin absorber structures.

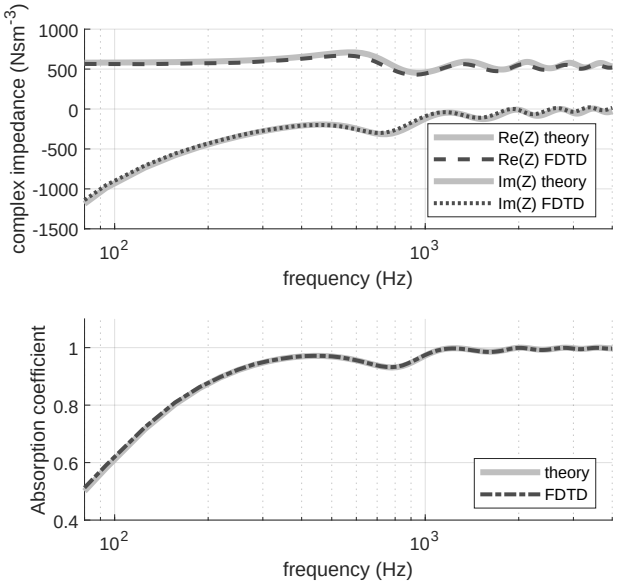

Figure 6: *Simulated impedance and absorption coefficient at interface of absorber for a plane wave at* 45° *incidence angle, with comparison to theory.*

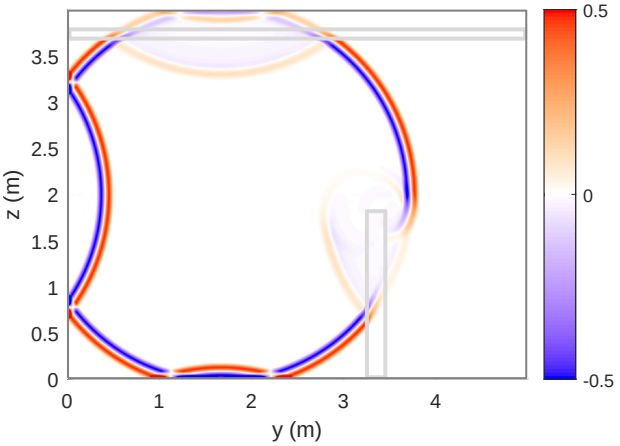

Figure 7: *Snapshot of acoustic wave propagation in a* $5\text{m} \times 5\text{m} \times 4\text{m}$ *(*100m^3*) benchmark room with ceiling absorber and free-standing porous panel, taken at* $t = 6\text{ms}$*. The colorscale is normalized to 50% of the maximum pressure values within the cross-section, giving some compression to improve visibility of the response around the porous volumes*

7. REFERENCES

[1] Lauri Savioja and Peter Svensson, "Overview of geometrical room acoustic modeling techniques," *J. Acoustical Society of America*, vol. 138, pp. 708–730, 08 2015.

[2] Osamu Chiba, Tatsuta Kashiwa, Hidemaro Shimoda, Shin Kagami, and Ichiro Fukai, "Analysis of sound fields in three dimensional space by the time-dependent finite-difference method based on the leap frog algorithm," *J. Acoustical Society of Japan*, vol. 49, no. 8, pp. 551–562, 1993.

[3] Lauri Savioja, Timo J. Rinne, and Tapio Takala, "Simulation of room acoustics with a 3-D finite difference mesh," in *Proc. Int. Computer Music Conf. (ICMC)*, Danish Institute of Electroacoustic Music, Denmark, 1994, pp. 463–466.

[4] Dick Botteldooren, "Finite-difference time-domain simulation of low-frequency room acoustic problems," *J. Acoustical Society of America*, vol. 98, no. 6, pp. 3302–3308, 1995.

[5] Lauri Savioja, "Real-time 3D finite-difference time-domain simulation of low- and mid-frequency room acoustics," in *Proc. Digital Audio Effects (DAFx)*, Graz, Austria, 2010, vol. 1, p. 75.

[6] Craig Webb and Stefan Bilbao, "Computing room acoustics with CUDA - 3D FDTD schemes with boundary losses and viscosity," in *Proc. IEEE ICASSP*, Prague, Czech Republic, 05 2011, pp. 317–320.

[7] Brian Hamilton, Stefan Bilbao, and Craig Webb, "Revisiting implicit finite difference schemes for 3-D room acoustics simulations on GPU," in *Proc. Digital Audio Effects (DAFx)*, Erlangen, Germany, 09 2014.

[8] Brian Hamilton, Craig Webb, Nathaniel Fletcher, and Stefan Bilbao, "Finite difference room acoustics simulation with general impedance boundaries and viscothermal losses in air: Parallel implementation on multiple GPUs," in *Proc. Int. Symp. on Music and Room Acoustics (ISMRA)*, Buenos Aires, Argentina, 09 2016.

[9] Konrad Kowalczyk and Maarten Van Walstijn, "Formulation of locally reacting surfaces in FDTD/K-DWM modelling of acoustic spaces," *Acta Acustica united with Acustica*, vol. 94, no. 6, pp. 891–906, 2008.

[10] Stefan Bilbao, Brian Hamilton, Jonathan Botts, and Lauri Savioja, "Finite volume time domain room acoustics simulation under general impedance boundary conditions," *IEEE/ACM Trans. on Audio, Speech, and Language Processing*, vol. 24, no. 1, pp. 161–173, 2015.

[11] Jean Allard and Noureddine Atalla, *Propagation of sound in porous media: modelling sound absorbing materials*, John Wiley & Sons, second edition, 2009.

[12] Cheol-Ho Jeong, "Guideline for adopting the local reaction assumption for porous absorbers in terms of random incidence absorption coefficients," *Acta Acustica united with Acustica*, vol. 97, pp. 779–790, 09 2011.

[13] Kristrún Gunnarsdóttir, Cheol-Ho Jeong, and Gerd Marbjerg, "Acoustic behavior of porous ceiling absorbers based on local and extended reaction," *J. Acoustical Society of America*, vol. 137, no. 1, pp. 509–512, 2015.

[14] Hisaharu Suzuki, Akira Omorto, and Kyoji Fujiwara, "Treatment of boundary conditions by finite difference time domain method," *Acoustical Science and Technology*, vol. 28, pp. 16–26, 01 2007.

[15] Nuno Ferreira and Carl Hopkins, "Using finite-difference time-domain methods with a Rayleigh approach to model low-frequency sound fields in small spaces subdivided by porous materials," *Acoustical Science and Technology*, vol. 34, no. 5, pp. 332–341, 2013.

Table 1: *Timing results for tests run on a RTX A5000 GPU at 32-bit floating-point precision. The room volume is 100m^3 and the simulation length is 1 second. The quoted frequency ranges correspond to a maximum numeric dispersion error of 2%.*

frequency range	6.2 kHz	20 kHz	
Cartesian grid spacing, h	10.0	3.07	mm
time step size, k	29.2	8.94	µs
total number of time steps	34.3	111.8	$\times 10^3$
domain sizes:			
total number of nodes	50.0	1725	$\times 10^6$
rigid boundary nodes	1.90	20.5	$\times 10^6$
porous volume nodes	1.25	46.1	$\times 10^6$
porous volume boundary nodes	0.55	6.0	$\times 10^6$
video RAM used	0.6	16.2	GB
timing results:			
air update	31.6	4456	secs.
rigid boundaries update	11.0	408	secs.
other (overhead)	3.3	93	secs.
internal porous volume update	7.8	711	secs.
porous boundary update	30.3	1168	secs.
total time for updates	83.9	6837	secs.

[16] Finnur Pind, Cheol-Ho Jeong, Allan P Engsig-Karup, Jan S Hesthaven, and Jakob Strømann-Andersen, "Time-domain room acoustic simulations with extended-reacting porous absorbers using the discontinuous Galerkin method," *J. Acoustical Society of America*, vol. 148, no. 5, pp. 2851–2863, 2020.

[17] Huiqing Wang and Maarten Hornikx, "General extended-reacting porous materials modeling with the time-discontinuous Galerkin method for room acoustic simulations," in *Proc. of the 24th Int. Congress on Acoustics*, Gyeongju, Korea, 2022.

[18] Jing Zhao, Zhifei Chen, Ming Bao, Hyojin Lee, and Shinichi Sakamoto, "Two-dimensional finite-difference time-domain analysis of sound propagation in rigid-frame porous material based on equivalent fluid model," *Applied Acoustics*, vol. 146, pp. 204–212, 2019.

[19] Antoni Alomar, Didier Dragna, and Marie-Annick Galland, "Time-domain simulations of sound propagation in a flow duct with extended-reacting liners," *Journal of Sound and Vibration*, vol. 507, pp. 116137, 2021.

[20] Konrad Kowalczyk and Maarten Van Walstijn, "Room acoustics simulation using 3-D compact explicit FDTD schemes," *IEEE Trans. on Audio, Speech, and Language Processing*, vol. 19, no. 1, pp. 34–46, 2010.

[21] Brian Hamilton and Stefan Bilbao, "On finite difference schemes for the 3-D wave equation using non-Cartesian grids," in *Proc. Sound and Music Computing Conf. (SMC)*, Stockholm, Sweden, 01 2013, pp. 592–599.

[22] Brian Hamilton and Craig J Webb, "Room acoustics modelling using GPU-accelerated finite difference and finite volume methods on a face-centered cubic grid," in *Proc. Digital Audio Effects (DAFx)*, Maynooth, Ireland, 2013, pp. 336–343.

[23] James Kates and Eugene Brandewie, "Adding air absorption to simulated room acoustic models," *J. Acoustical Society of America*, vol. 148, pp. EL408–EL413, 11 2020.

[24] Brian Hamilton, "Air absorption filtering method based on approximate Green's function for Stokes' equation," in *Proc. Digital Audio Effects (DAFx)*, 2021, pp. 160–167.

[25] Kane Yee, "Numerical solution of initial boundary value problems involving Maxwell's equations in isotropic media," *IEEE Trans. on Antennas and Propagation*, vol. 14, no. 3, pp. 302–307, 1966.

[26] John C Strikwerda, *Finite difference schemes and partial differential equations*, SIAM, Philadelphia, PA, second edition, 2004.

[27] Jonathan Botts and Lauri Savioja, "Integrating finite difference schemes for scalar and vector wave equations," in *Proc. IEEE ICASSP*. IEEE, 2013, pp. 171–175.

[28] M.E. Potter, M. Lamoureux, and M.D. Nauta, "An FDTD scheme on a face-centered-cubic (FCC) grid for the solution of the wave equation," *J. Computational Physics*, vol. 230, no. 15, pp. 6169–6183, 2011.

[29] Julie Meyer, Tapio Lokki, and Jens Ahrens, "Perceptual detection thresholds for numerical dispersion in binaural auralizations of two acoustically different rooms," *J. Acoustical Society of America*, vol. 152, pp. 2266–2276, 10 2022.

[30] Jean-F. Allard and Yvan Champoux, "New empirical equations for sound propagation in rigid frame fibrous materials," *J. Acoustical Society of America*, vol. 91, no. 6, pp. 3346–3353, 1992.

[31] Didier Dragna, Pierre Pineau, and Philippe Blanc-Benon, "A generalized recursive convolution method for time-domain propagation in porous media," *J. Acoustical Society of America*, vol. 138, no. 2, pp. 1030–1042, 2015.

[32] Antoni Alomar, Didier Dragna, and Marie-Annick Galland, "Pole-based identification method to extract the equivalent fluid characteristics of general sound-absorbing materials," *Applied Acoustics*, vol. 174, 12 2020.

[33] Bjørn Gustavsen and A. Semlyen, "Rational approximation of frequency-domain responses by vector fitting," *IEEE Trans. on Power Delivery*, vol. 14, pp. 1052 – 1061, 08 1999.

[34] Brian Hamilton, "Finite volume perspectives on finite difference schemes and boundary formulations for wave simulation," in *Proc. Digital Audio Effects (DAFx)*, 2014, pp. 295–302.

[35] Brian Hamilton, "PFFDTD software," 2021, https://github.com/bsxfun/pffdtd.

[36] Ken Museth, "VDB high-resolution sparse volumes with dynamic topology," *ACM Trans. on Graphics*, vol. 32, pp. 27:1–27:22, 07 2013.